Chinese Chemical Letters 34 (2023) 107322

Contents lists available at ScienceDirect

Chinese Chemical Letters

journal homepage: www.elsevier.com/locate/cclet

A mussel-induced approach to secondary functional cross-linking 3-aminopropytriethoxysilane to modify the graphene oxide membrane for wastewater purification

Wenwen Tu[a], Yucheng Liu[a,b,*], Mingyan Chen[a,b], Lili Ma[a,b], Lingli Li[a,b], Bing Yang[a,b]

[a] College of Chemistry and Chemical Engineering, Southwest Petroleum University, Chengdu 610500, China
[b] Research Institute of Industrial Hazardous Waste Disposal and Resource Utilization, Southwest Petroleum University, Chengdu 610500, China

ARTICLE INFO

Article history:
Received 6 December 2021
Revised 23 January 2022
Accepted 10 March 2022
Available online 13 March 2022

Keywords:
Cross-linked graphene oxide
Polydopamine
APTES
High flux membranes
Dye separation

ABSTRACT

Graphene oxide (GO) with one-atom-thick exhibit remarkable molecule sieving properties, but its low permeance flux renders it difficult to be applied in practice as a high-permeance separation membrane. In this study, we design complex membrane from covalently crosslinked GO, polydopamine (PDA), and 3-aminopropytriethoxysilane (APTES) as building blocks to fabricate the high-permeance GO-based membrane *via* the vacuum filtration method. A branched crosslinking product (PDA/APTES) working as a clamp grasped the hydrophilic functional groups (hydroxyl, epoxy, carboxyl) on GO for improving the GO membrane flux. The interlayer structure of the GO membrane was optimized according to the crosslinker concentration, reaction time, initial pH, and temperature for RGO/PDA/APTES (RGPA) in this study. At the optimized reaction conditions including the crosslinker concentration of 1.4 mL/L, the temperature of 80 °C, the time of 16 h, and the initial pH of 8.5 for RGPA mixture, the interlayer gallery of RGPA membrane was effectively tunes, endowing high flux ranging from 11.98 L m^{-2} h^{-1} to 1823.97 L m^{-2} h^{-1}. Besides, the RGPA membrane ensured the high rejections to dye solutions such as methylene blue (MB) (>99%) and congo red (CR) (>90%). Meanwhile, the superior reusable performance of the RGPA membrane was achieved, together with the rejections for MB and CR to 96.32% and 93.1% after 4 cycles, respectively. Also, the RGPA membrane possessed superior anti-fouling performances for bovine serum albumin (BSA) aqueous solution and excellent stabilities in harsh conditions (pH 3, 7 and 11). Grafting the crosslinker onto GO nanosheets exhibits the distinct advantages of achieving the high flux, high rejections to dyes, and superior reusable performance of membranes, posing a great application potential for membrane separation technology in wastewater treatment.

Water ecological environment problems have gained much attention with the development of society and industry. The common treatment approach for wastewater mainly focuses on the membrane technology, catalysis, and biology technologies to achieve the separation and degradation of wastewater [1–5]. Here, membrane separation technology has been widely used due to its merits such as high-efficiency and low capital costs. A great number of recent investigations focus on the assembly of two-dimensional (2D) membrane materials to the effective transport of liquid, gases, ions, and other species [6]. Graphene oxide (GO), a typical 2D material, has many breakthrough research and applications in electronics, catalysis, and energy storage because of its large surface area and exceptional mechanical, optical, and thermal properties. Based on its unique 2D nanosheets structure, GO is considered as one of the most favorable candidates to be fabricated as the laminate membrane, whose interlayer galleries are a fundamental platform to provide special molecular transport. Graphene oxide membranes have been explored for their superior molecular transport and separation properties in wastewater treatment applications [7–9]. While, the GO membranes have been confronted with issues such as low water permeance, which need to be further worked out [10].

Many attempts have been applied to ameliorate the flux and selective separation performances of GO based membranes. For example, some efforts such as tailoring the interlayer galleries [11,12], intercalating the nanomaterial [13,14], and preparation the nano-porous [15] on the GO nanosheets have been put forward to address the above issues. An effective and straightforward approach to enhance the flux aims at creating the pores on the GO

* Corresponding author.
E-mail address: rehuo2013@sina.cn (Y. Liu).

https://doi.org/10.1016/j.cclet.2022.03.045
1001-8417/

nanosheets. Kim *et al.* adopted the potassium hydroxide activation of graphite to prepare a kind of impenetrable and confined GO membranes. The fabricated GO films exhibited an enhanced pure water flux (PWF) of 37 L m^{-2} h^{-1} bar^{-1}, which reached six times higher than that of the regular GO membrane [15]. However, the preparation process of nanoporous graphene *via* the Scotch tape method or chemical vapor deposition (CVD) requires very extremely strict control, which is restricting its extensive applications [16]. Incorporating the intercalation material has also proven to be an acceptable approach to enhance permeance. According to our previous study, UiO-66, acting as an intercalation material, endowed the modified PDA/RGO/UiO-66 membrane with the PWF of 167.14 L m^{-2} h^{-1}, being an increase of 256.91% over that of the original PDA/RGO membrane [17]. Similarly, Zeng *et al.* designed the membrane integrated with hybrid GO, UiO-66-NH_2, and polyacrylic acid (PAA). The PWF value of GO/UiO-66-NH_2/PAA was 100 L m^{-2} h^{-1}, which led to 6.6 times flux comparing to that of the pure GO membrane [18]. Nevertheless, an increase in permeance in the previous research was much lower than expected because the excess intercalation materials might block the molecular transport passages [17,19]. Another GO membrane modification method is the cross-linking modification method, containing a function of cross-linker to adjust the interlayer gallery of GO nanosheets. Valizadeh *et al.* utilized the heterobifunctional crosslinker role for β-alanine to fabricate the GO nanosheets. The modified GO membrane provided a PWF value of 732 L m^{-2} h^{-1} with a superior removal efficiency for Penicillin-G procaine [20]. Lu *et al.* designed the modified GO membrane by increasing the interlayer space of GO nanosheets by grafting the poly (ethylene imine), which exhibited the flux up to 450.2 L m^{-2} h^{-1} bar^{-1}, being 20 times higher than that of the original GO membrane [21]. Hence, a strategy to fabricate the GO nanosheets *via* the role of cross-linker has been deemed as an effective approach and method to tune the interlayer galleries of GO nanosheets.

Recently, the membranes fabricated by the mussel-inspired method *via* the covalent crosslink approach have been extensively discussed [22,23]. Among the mussel materials, dopamine, as a kind of natural melanin, is equipped with numerous notable properties such as chemical reactivity, electrical conductivity, adhesive, metal ions redox activities, and biocompatible and biodegrade [24]. A prominent feature of PDA consists in its special physical and chemical structure that embodies several functional groups, which act as primary actives (catechol, amine, and imine) for further modifications [24]. With such benefits, PDA is feasible for applications across the chemical, physical, and material science. In recent studies, polydopamine has been used in the surface modification of materials due to its special adhesion properties [17,25]. The adhesive property, redox activity, and chemical reactivity of PDA pave a versatile way and provide a secondary reaction platform for the construction of composite material with specific functionality. In general, amine groups and carboxylic groups are ideal cross-linker to covalently integrate with GO nanosheets [26,27]. However, the GO membranes modified by the individual polydopamine exhibited poor effects on the enhancement of permeance [13,17]. Hence, to prompt the permeance of the GO based membrane, an expection to chemically fabricate the PDA *via* binding with a secondary functionalized monomer is optional. Typically, the –NH_2 and –OH functional groups on PDA could work as the active sites and react with secondary functionalized monomers. APTES, as a class of conventional silane coupling agents, is composed of abundant hydroxyl, siloxane, silanol, and amine groups [28], which are counted on integrating with GO and PDA *via* the role of chemical bonds. Gu *et al.* designed anchoring the graphene oxide quantum dots on the APTES functionalized alumina membrane to prepare the composite membrane, which exhibited improvement hydrophilicity and permeability [29]. Ma *et al.* synthesized the halloysite material modified by APTES, which acted as the intercalation material for GO membrane, showing satisfactory stability and water permeability (159.40 L m^{-2} h^{-1}) [30]. Hence, APTES is an ideal candidate to act as a crosslinker. Many previous studies [31,32] related to the anti-corrosion and surface modification performances on PDA and APTES have focused on the secondary functionalized monomer modification on PDA to elevate the permeance of the GO membrane. Hence, the way *via* the secondary functionalized monomer modification on PDA/GO is a possibly pathway to adjust the interlayer gallery for GO membrane and enhance the flux of the GO membrane.

In this study, the grafting of the crosslinker APTES to bond with PDA was designed. Several active sites supplied by PDA/APTES composites provided opportunities to react with GO. By the secondary functionalized monomer modification on PDA, the interlayer gallery of GO composites was significantly tuned. The hybrid RGPA composites were assembled into a stacked RGPA membrane *via* the vacuum filtration on the commercial cellulose acetate membrane (CAM). The as-prepared RGPA composite and RGPA membrane were characterized. Furthermore, the preparation conditions of the RGPA mixture such as the dosage of APTES, reaction temperature, time, and initial pH were optimized to explore their influences on the separation and permeance performance for the membrane. Typically, the reaction and synthesis mechanism among GO, PDA, and APTES was explored. Meanwhile, the pH of dye solution, the effects of filtration amount, and the concentration of dye solution on the membranes' separation performances were also discussed. Finally, the reusable experiments of the membrane were also carried out.

Here, the details of reagents and materials were shown in Text S1 (Supporting information). The details of preparation of RGO/PDA/APTES composite were shown in Text S2 (Supporting information). As for the synthesis of RGPA membrane, the preparation of the RGPA membrane was carried out by the dead-end equipment, which was equipped with a vacuum pump and filter cup (YuHua Equipment Factory, Gongyi, China) (depicted in Fig. S1 in Supporting information). Specifically, the synthesized 4 mL of the RGPA mixture was diluted to 100 mL with DI water. Then, 25 mL of dispersion was filtrated on the cellulose acetate membrane (a diameter of 5 cm × 5 cm and average pore sizes of 0.22 μm) at 0.09 MPa. A specific preparation procedure of the modified membrane was shown in Fig. 1.

Moreover, the characterization of materials and membrane filtration performance methods were shown in Texts S3 and S4 (Supporting information).

The FT-IR spectrums for PDA, GO, RGP, RGA, and RGPA were measured to explore the functional groups of samples, as shown in Fig. 2a. In the FT-IR spectra of PDA, the N–H (3300 cm^{-1}) stretching, C=N (1629 cm^{-1}) bond stretching, and C–N (1396 cm^{-1}) [33–35] stretching peaks were visible, which illustrated that the polymerization reaction of dopamine occurred in the RGPA mixture at a temperature of 80 °C, and pH of 8.5 [24]. For the FT-IR spectrums of GO, the typical absorption bands included the O–H at 3429 cm^{-1}, C–H at 2889 cm^{-1}, C=O at 1724 cm^{-1}, C=C at 1618 cm^{-1}, C−OH at 1409 cm^{-1}, C–O at 1225 cm^{-1} (epoxy) and C–O (alkoxy) at 1048 cm^{-1} [13,20,36–38]. The spectrum of RGA showed intense peaks for Si−O−C and Si−O−Si at 1103 cm^{-1} and 1027 cm^{-1}, indicating the successful grafting for APTES on GO [39,40]. For the spectrum of RGPA, some similar characteristics such as N–H, C–O, Si−O−Si, C–N, and C=N were also observed, verifying the binding of PDA and APTES with GO. The abatement of the intense peak for GO at 1724 cm^{-1} corresponding to C=O on carboxyl and the appearance of −CONH at 1583 cm^{-1} were due to the reaction between −COOH on GO and amide functional groups on DA or APTES [39,41,42]. The XRD patterns of GO, RGA, RGP, and RGPA were also analyzed to verify the crystal structure, interlayer structure, and re-

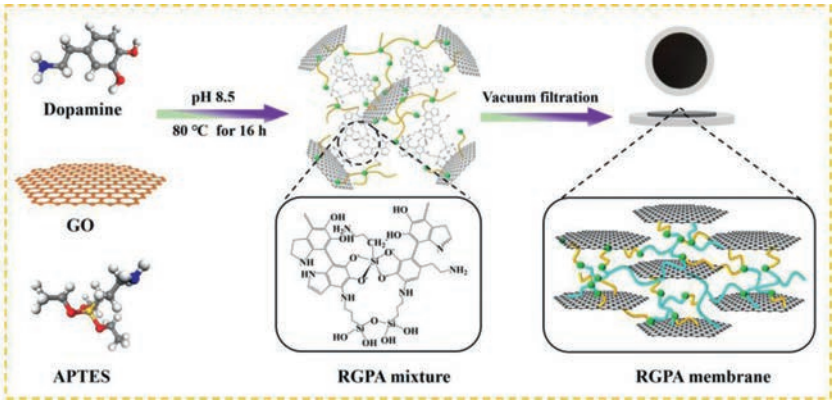

Fig. 1. Preparation procedure of the RGPA membrane.

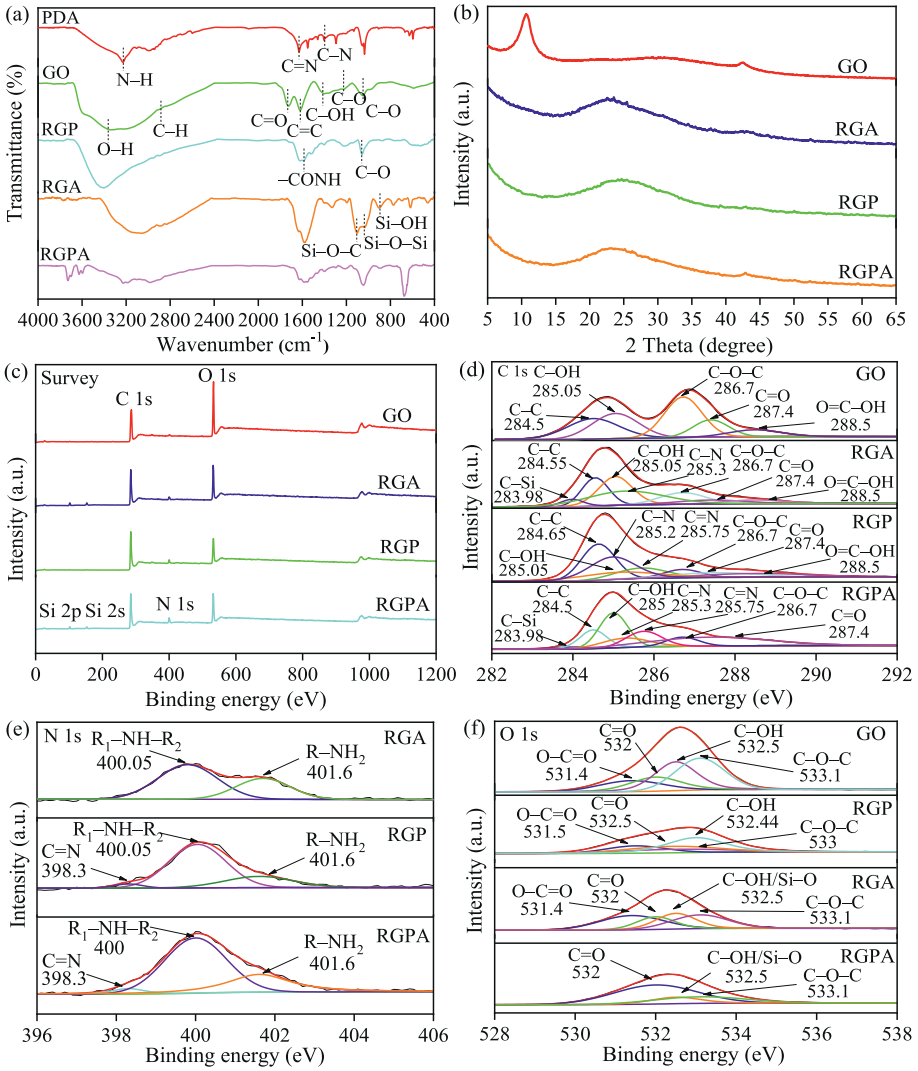

Fig. 2. (a) FTIR spectra of PDA, GO, RGP, RGA and RGPA. (b) XRD patterns of GO, RGP, RGA and RGPA samples. (c) XPS survey spectra for GO, RGA, RGP and RGPA. (d) C 1s spectra in XPS for GO, RGA, RGP and RGPA. (e) N 1s spectra in XPS for RGA, RGP and RGPA. (f) O 1s spectra in XPS for GO, RGP, RGA and RGPA.

duction effect of GO-based materials. Fig. 2b demonstrates that the pure GO with a diffraction angle at 2θ=10.67° corresponded to the D-spacing for 0.83 nm according to the Bragg equation, in agreement with our previous studies [13]. When GO was mixed with APTES, PDA, and PDA/APTES composites, the characteristic diffraction angle at 2θ=10.67° was disappearance. Meanwhile, the typical diffraction angles of RGA, RGP, and RGPA near 2θ=24° manifest the successful reduction of GO (RGO) *via* chemicals and revealed the RGPA membrane was loosely stacked [43]. In addition, the XRD patterns were also a straightforward approach to reflect the swelling effect of membrane. As seen in the Fig. S4 (Supporting information), the diffraction angle for RGPA membrane in wet state

demonstrated the similar state compared to the dry RGPA. Moreover, the Raman spectra were used to detect the structure properties of GO and RGPA (Fig. S5 in Supporting information). Here, the intensity ratio of D-band (I_D) and G-band (I_G) reveals the extent of disorder for graphene oxide including sp^3 defects and sp^2 hybridized. In this work, the GO and RGPA materials occupied two peaks at 1320 cm^{-1} (D band) and 1580 cm^{-1} (G band), corresponding to the I_D/I_G for 1.009 and 1.046, respectively. The increase of I_D:I_G values illustrated the enhanced graphitization (the conversion from sp^2 to sp^3), and the increase of disorder extent and defect of RGPA because of the functionality and reduction of GO [44–46]. Moreover, the BET specific surface area for GO and RGPA composite is 192.3682 m^2/g and 10.5760 m^2/g, respectively. It could be seen that the reduction process decreased the BET surface area of GO. This is consistent with previous investigation [47,48]. Based on the IUPAC classifications of physisorption isotherms and associated hysteresis loops, the GO and RGPA materials corresponds to type I and type III isotherms (Fig. S6 in Supporting information). These results revealed that the GO material was composed of micropores and the RGPA material contained the relative weak adsorption effect between adsorbent and adsorbate [49].

The surface elemental compositions of GO, RGA, RGP, and RGPA were examined by XPS analysis (Figs. 2c-f). Table S1 (Supporting information) summarizes the proportion corresponding to the C, N, O and Si elements in all samples. As shown in Fig. 2c, the wide survey spectrums of GO, RGA, RGP and RGPA samples exhibited the presence of C and O atoms. The N atoms emerged in RGA, RGP, and RGPA composites, respectively. Si atoms were detected in RGA and RGPA samples. The XPS C 1s emission of GO (Fig. 2d) can be Gaussian deconvoluted into five peaks, assigning to the C–C (284.5 eV), C–OH (285.05 eV), C–O–C (286.7 eV), C=O (287.4 eV), and O=C–OH (288.5 eV), respectively [36]. The C 1s high-resolution spectra of RGP and RGA can also be fitted into C–Si (283.98 eV), C–N (285.3 eV), and C=N (285.75 eV) besides the above peaks [13,34], verifying the occurrence of the cross-linking reaction [19]. The C–N peaks stemmed from APTES or PDA, and the C=N peak was from the self-polymerization of dopamine. Particularly, the peaks for C–O–C and C–OH in modified GO materials decreased in strength compared to pure GO due to the cross-linking reaction between GO and PDA&APTES [50,51]. Moreover, the C/O ratio shown in Table S1 increased in RGA, RGP, and RGPA due to the loss of oxygen during the crosslink reaction [52]. The main peaks of centering at 398.3 eV, 400.05 eV, and 401.6 eV in the N 1s region of XPS spectra (Fig. 2e) were attributed to C=N, R_1–NH–R_2, and R–NH_2, respectively [17,53]. With the modification by PDA&APTES for RGPA membrane, the content of R–NH_2 decreased, that of the R_1–NH-R_2 increased, and that of C=N nearly keeps stable. This demonstrated that the cross-linking reaction between –NH_2 on APTES and PDA was *via* the Michael-type addition pathway [24]. Fig. 2f shows the Gaussian curve-fitting peak of O 1s for GO, RGA, RGP and RGPA. Specifically, the curve-fitting peak of O 1s could be fitted into O–C=O (531.4 eV), C–OH (532.5 eV), C–O–C (533.1 eV), and C=O (532 eV) for pure GO. When modified by PDA and APTES, the peak intensity of O 1s on RGPA material decreased significantly, which might be caused by the cross-linking effect of GO. Overall, the presence of typical bands of PDA, APTES, and GO in the RGPA samples indicated that the composites were fabricated as designed. The curve-fitting results for C, N and O elements in XPS spectra confirmed the cross-linking interactions among GO, PDA, and APTES.

The surface morphology and cross-section images of GO, RGA, RGP, and RGPA were characterized by SEM. The pure GO for the surface morphology in Fig. 3a showed the majority of resembling twist wrinkled corrugations, which was formed by the hydrogen bond interactions among the hydrophilic functional groups on the GO [6]. The degree of wrinkling of the GO membrane is alleviated after modification by PDA or APTES (Figs. 3b and c). It is probably caused by two reasons. First, the GO was reduced by PDA or APTES together with the decrease of hydrophilic oxygen-containing functional groups. Hence, the interaction effect between the basal plane and edges of GO membrane tended to be abatement. Second, the probable hydrogen bond, electrostatic, and π-π interactions between APTES or PDA chemicals and GO membrane could occupy more active sites and hence restrain the wrinkled tendency of GO membrane. The aggregated wrinkled corrugations are obvious *via* the fabrication of PDA and APTES composites (Fig. 3d). It demonstrated that the cross-linking interactions between the –COOH, C–OH, C–O (epoxy) on the edge and basal planes of GO, and –NH_2, –OH functional groups on PDA/APTES composites might expand the corrugations extents. The AFM characterizations were used to verify this phenomenon. The R_s (66.498 nm) and R_a (55.854 nm) values of GO are lower than that of RGPA membrane (R_s: 160.087 nm; R_a: 125.874 nm) (Fig. S7 in Supporting information), which indicates the enhancement of roughness for modified GO membrane. Furthermore, the wrinkled corrugations of the GO membrane were almost homogeneously distributed, whereas the RGPA membrane demonstrated incoherent corrugations. For the cross-section images of modified GO membrane, the accumulation state of the membrane had an obvious discrepancy. The pure GO membrane demonstrated a tight stacked state with a thickness of 254.7 nm (Fig. 3e). With the modification of PDA or APTES, the thickness of the membrane has greatly increased from 254.7 nm to 1.369 μm for GO and RGPA membrane (Figs. 3f-h). On the one hand, we speculated the enhancement of thickness for membranes might be due to the increase of interlayer space. According to our XRD results as mentioned above, there was no obvious decrease of diffraction angle when they were from 5° to 65° for RGP, RGA, and RGPA samples. Hence, the XRD characterizations of small diffraction angle for RGP and RGPA were carried out. It could be seen (Fig. S8 in Supporting information) that there were no diffraction peaks at 2θ from 1° to 10° for both samples. Therefore, it is unsuitable to explain this phenomenon *via* the increase of interlayer space based on the results calculated by the XRD patterns. On the other hand, it was conjected that this was due to the irregular stacking of the reduced GO membrane through the cross-linking fabrication of GO, PDA and APTES. Particularly, optical microscope was used to detect the stacking state, distribution, and light transmittancy extent of modified GO membrane on CA substrate. Some phenomenon could be observed from Fig. S9 (Supporting information) that the single light was bright and dazzling. The pure GO membrane demonstrated the lighttight and brown membrane. After modified by PDA, some dark spots were noticed on the lighttight RGP membrane, due to the decrease of oxygen-containing functional groups and the increase of the agglomeration of reduced graphene oxide. After modified by APTES, some undistributed flake agglomerates were observed on the surface of lighttight RGA membrane because of cross-linking and reduced effects of APTES. However, the obvious phenomenon with chunk agglomerates were seen for RGPA membrane. This was due to that the cross-linking product between PDA and APTES grasped the GO and reduced the GO membrane. Hence, we could conclude that the increase of membrane thickness was attributed to the drastic restore of graphene oxide, which brought down the dispersion of GO in aqueous solutions, brought out the agglomeration RGO membrane, and further caused the irregular stacking of RGO membrane.

The EDS mapping of the RGPA membrane is characterized to explore the distribution of elements, as shown in Figs. 3i-m. Some elements such as C, N, O, and Si were distributed on the surface of the membrane. This is consistent with the XPS analysis that the primary elements are C, N, O, and Si in the RGPA composite.

No studies have been conducted to determine the complicated formation mechanism of PDA and APTES oligomers. In this study,

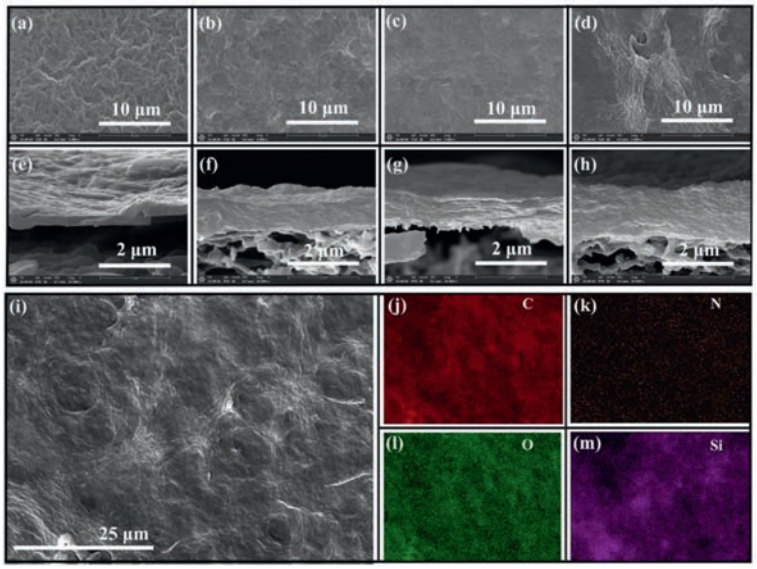

Fig. 3. SEM morphologies of (a) GO, (b) RGA, (c) RGP and (d) RGPA. Cross-section morphology of (e) GO, (f) RGA, (g) RGP and (h) RGPA. (i-m) EDS mapping of RGPA membrane.

the proposed structure of RGPA was postulated based on the characterization results and previous research. Specifically, the probable interactions between dopamine and APTES mainly concentrate on the hydrolysis of APTES, self-polymerization of dopamine, condensation, and Michael's addition reactions between APTES and dopamine (Fig. S10 in Supporting information). First, for the APTES in the mixture, the alkoxy on the APTES could be hydrolyzed into silanol, which could further proceed with the condensation reaction (1) [34,54]. It was verified by the FTIR results that functional groups such as Si–O–Si, and Si–OH were characterized on the RGPA. Second, for the dopamine in the mixture, it occurs a series of polymerization reactions such as oxidation, rearrangement, Michael addition. For example, under alkaline conditions, dopamine is oxidized to dopamine quinone followed by the cyclization reaction to the yield of leucodopaminechrome. Subsequently, leucodopaminechrome undergoes oxidation and rearrangement reactions to form the 5,6-dihydroxyindole (DHI). The products continue to undergo the branch reaction at the positions of 2, 3, 4 and 7 to the formation of the oligomerization products (reaction (2)) [24,35]. The observed emergence of C–N and C=N bonds in the FTIR of PDA, RGP, and RGPA samples, and the appearance of peaks corresponding to C–N and C=N bonds in the XPS spectrum approved the formation of oligomerization products. Third, according to the previous study, the Schiff base and Michael addition reactions usually occurred between PDA and APTES [25,34,35]. Based on the hydrolysis of APTES and polymerization reactions of dopamine, the dopamine quinone can also react with the free amine in APTES to form the monomeric unit *via* the Michael addition (3) [55]. This can be explained by the N 1s high-resolution spectrum of RGP and RGPA. Since the Schiff base reactions of RGP and RGPA might lead to the variation of peak intensity for C=N bonds. While the Michael addition pathway could not form the C=N bonds. In this study, the peak intensity of C=N remains stable, which revealed Michael's addition is dominating. Furthermore, it is noted that the condensation reaction between APTES and catechol in dopamine or polydopamine molecule also forms the pentacoordinate silicon complexes (reaction (4)) [56]. According to the above results, it was speculated that a similar network polymer structure was formed *via* the secondary crosslinking reaction between APTES and polydopamine. These functional groups such as amino, hydroxyl on polymers could further crosslink with GO as a function of hydrogen or electrostatic interaction. The binding ration of composite was verified by TG measurements for RGP and RGPA composites [57–59]. It can be seen from Fig. S11 (Supporting information) that when the temperature ranges from 200 °C to 500 °C, an obvious discrepancy of residual mass for RGP and RGPA composite are observed. In this stage, the residual mass for RGP and RGPA composite were 83% and 86.6%, respectively, suggesting that 3.6% APTES was binding with RGP composite.

The observation of a reduction in peak intensity of C–O–C, C=O and COOH emissions for RGA, RGP and RGPA in C 1s spectrums of XPS demonstrated the cross-linking effects in the reaction mixture. Specifically, a typical absorption band of –CONH at 1583 cm^{-1} for the RGP sample revealed the probable interactions (*i.e.*, amidation reaction) between $-NH_2$ on PDA and –COOH on GO [20]. Furthermore, the peak intensity and related content of epoxy groups in the C 1s and O 1s emission of RGPA material demonstrated a significant decrease in Figs. 2d, f and Table S1. This may due to the reaction between an epoxy ring on GO and a primary amine on PDA/APTES [60].

Wettability and permeance of the membrane are key factors to evaluate membrane properties. The pure water permeance for GO laminated membrane was related to its hydrophilicity, nanochannels, and inner wrinkle and defects [61]. The measurement of water contact angle is a pathway to evaluate the hydrophilicity and hydrophobicity of membranes. A WCA value below 90° indicates that the surface is hydrophilic, while that above 90° is that the surface is hydrophobic [18]. The WCA values of GO, RGP, RGA, and RGPA (M2) were examined in this study (Fig. S12a in Supporting information). The results showed that the WCA value of pure GO was 43.9°, which demonstrated the hydrophilic property of the GO membrane [62,63]. As modified by PDA, the WCA values for RGP membrane increased to 72.4°, being attributed to the reducing of oxygen-containing functional groups. While, when it was combined with APTES, PDA and GO composite, the WCA value of membrane decreased to 56.1° because of the addition of hydrophilic functional groups on APTES (–OH, Si–O, and $-NH_2$ groups). However, the hydrophilicity for RGPA membrane was a little bit decline in comparison to GO membrane. On the one hand, this might be ascribed to the cross-linking reaction of GO with APTES and PDA, and hence cause a decrease of hydrophilic oxygen-containing func-

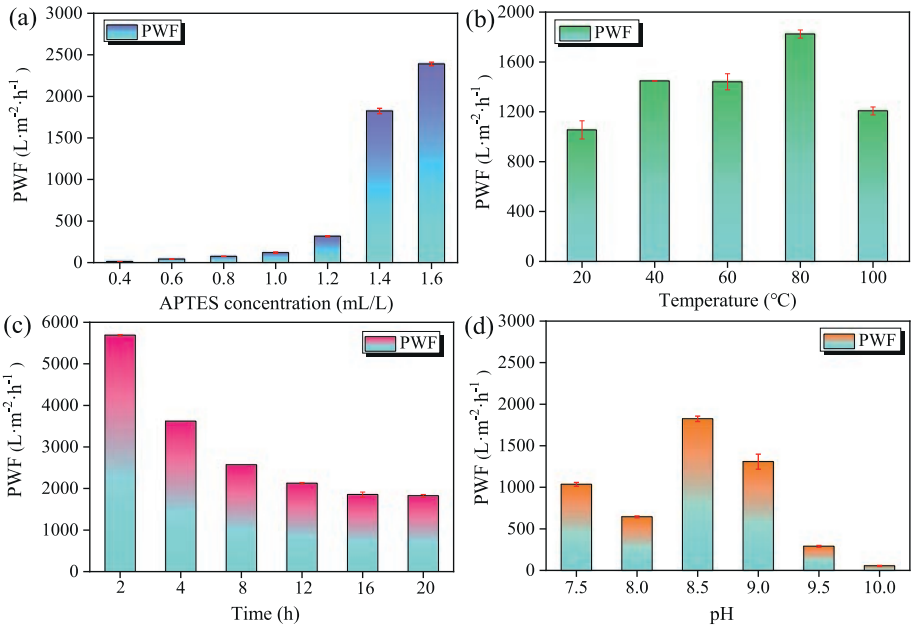

Fig. 4. The influences of (a) APTES concentration, (b) reaction temperature, (c) reaction time, and (d) reaction pH for RGPA mixture on the permeability performance of pure water flux.

tional groups on GO. On the other hand, it could be due to the increase of surface roughness and the formation of pores on the RGPA membrane [64]. In addition, the water permeance is positively related to the water flow channel, and inner wrinkle and defects for GO based laminated membranes, which is evaluated by the PWF values of membranes [65]. Here, GO, RGP, and RGPA (0.8 mL/L) composite were homogeneously dispersion. On the contrary, the cross-linker with high concentration induced the serious crosslink interaction for RGA and RGPA (1.4 mL/L). The PWF values corresponding to GO, RGP, RGA (1.4 mL/L), RGPA (0.8 mL/L-M1), RGPA (1.2 mL/L), and RGPA (1.4 mL/L-M2) membranes were 7.96 L m^{-2} h^{-1}, 18.96 L m^{-2} h^{-1}, 61.24 L m^{-2} h^{-1}, 74.99 L m^{-2} h^{-1}, 316.67 L m^{-2} h^{-1}, and 1823.97 L m^{-2} h^{-1}, respectively (Fig. S12b in Supporting information). The PWF of the RGPA membrane (M1 and M2) was greatly improved due to the irregular stacking and more defects in the laminated membrane. While, the water permeance for RGA (61.24 L m^{-2} h^{-1}) and RGPA (1823.97 L m^{-2} h^{-1}) demonstrated the obvious differences at the similar CA values (similar wettability for water). Hence, these results indicated the water flow nanochannel, membrane roughness, and hydrophilic played crucial roles in the transport of molecular through the GO-based membrane in this study [66].

The separation property of the membrane is related to the inner structure of RGPA materials, which is affected by the preparation conditions such as cross-linker concentration, reaction time, temperature, and initial pH. The single factor alternative method was used to optimize preparation conditions. First, various concentrations of APTES (0.4, 0.6, 0.8, 1, 1.2, 1.4, and 1.6 mL/L) were tested for optimization at the temperature of 80 °C, the reaction time of 16 h and the initial pH of 8.5. The RGPA membrane modified by 1.6 mL/L of APTES exhibited 198 times enhancement of PWF than that modified by the 0.4 mL/L of APTES (Fig. 4a). It could be the results of the following two reasons: One reason could be that as an increase of APTES dosage, the PDA/APTES occupied more active sites to crosslink with GO *via* the edge and basal planes, increasing the interlayer space and improving the pure water flux, which has been verified by SEM analysis. The other reason could be that the transport pathway of molecular in the GO membrane was mainly based on the slip flow theory, which indicated the molecular transport was along with the non-oxidized and nearly frictionless surface [6]. As mentioned above in the XPS analysis, the content of oxygen-containing functional groups on GO were decreased through the cross-linking reaction of PDA and APTES. Therefore, the interaction effects between GO membrane and water molecular were reduced which facilitated the flow of water in the interlayer. Thirdly, as Fig. S9 demonstrated, some inner defects which prompted the water permeability were observed on the membrane surface.

Furthermore, MB and CR solutions of 50 mg/L were further used to explore their retention performances (Figs. S13a and b in Supporting information). The flux variations of MB and CR were similar to the pure water flux. All the membranes exhibited superior rejections for MB solutions with a 98% removal efficiency. When the concentration of APTES is lower than 1.4 mL/L, the CR rejections for the RGPA membrane were higher than 98%. However, when it was higher than 1.4 mL/L, the CR rejections for the RGPA membrane were lower than 90%. The rejection mechanism of dye molecules for the RGPA membrane is a function of physical sieving, electrostatic, hydrogen bond, and π-π interactions [18]. An enhancement of interlayer space prompts the transport speed of molecular in the interlayer gallery of RGPA membrane while decreasing the contact opportunity during the filtration process. However, a sufficiently large enough space played an adverse role in the retention of dye molecular based on the physical sieving effects. To further discuss the effects of reaction factors and improve the separation permeance of the RGPA membrane, the APTES concentration of 1.4 mL/L was selected for the subsequent optimal experiments to explore the key influence factors during the preparation process.

The effect of preparation temperature (20 °C, 40 °C, 60 °C, 80 °C, and 100 °C) was also explored at the condition of 1.4 mL/L of APTES, 16 h and pH 8.5. The RGPA membrane prepared from the mixture heating at 80 °C has a 72.92% higher pure water flux than that of the membrane heating at 20 °C (Fig. 4b).

The rejection efficiencies of MB were stable and above 98% under the reaction 20 °C to 80 °C, while the rejection efficiencies of CR increased from 66.23% to 90.18% as the temperature increased from 20 °C to 80 °C (Figs. S13c and d in Supporting information), which may be caused by the lower cross-linking extent of RGPA

mixture heating at 20 °C [67]. Furthermore, the self-polymerization of DA and the increase of PDA layers could be accelerated by increasing the reaction temperature [68]. Due to the rejections and permeance of RGPA membranes, the preparation temperature of 80 °C was selected for further optimal experiments.

The effects of reaction time (2, 4, 8, 12, 16, and 20 h) for the RGPA mixture were examined for optimization at the condition of 1.4 mL/L of APTES, 80 °C, and pH 8.5. The PWF value of the RGPA membrane for different preparation times was explored. Generally, the increase of reaction time is not favorable to the permeance of pure water. It was observed from Fig. 4c that the PWF values of the RGPA membrane reduced from 5686.99 L m^{-2} h^{-1} to 1852.58 L m^{-2} h^{-1} corresponding to the reaction time increasing from 2 h to 16 h.

At the same conditions, the separation performances of MB and CR solutions were discussed. The rejection performances of MB solutions were above 99%, whereas the CR ranged from 73.48% to 92.2% with the reaction time from 2 h to 20 h. During the preparation process, the color of the RGPA solution at 2 h turned from brown to black-brown. It is possibly caused by reaction time that is inadequate for the formation of cross-linking products. The RGPA solution is a mixture of GO, DA, and APTES, which act as a poor role in the rejections of CR molecules due to the electrostatic repulsion. Meanwhile, the fluxes gradually declined from 3927.89 L m^{-2} h^{-1} to 1244.02 L m^{-2} h^{-1} for MB, and from 3895.26 L m^{-2} h^{-1} to 1577.87 L m^{-2} h^{-1} for CR, respectively (Figs. S13e and f in Supporting information). This result may be due to the filter cake on the membrane surface and the blocked interlayer channels that hinder the permeation of dye solutions [69]. Here, based on the rejections and permeance of RGPA membranes, the preparation time of 16 h was chosen as the preparation time to optimize the reaction.

Besides the dosage of APTES, and the reaction temperature and time, initial pHs (7.5, 8, 8.5, 9, 9.5, and 10) of reaction aqueous solutions are also important to impact the crosslink extent of RGPA. The different pH environments of aqueous solutions could activate different binding sites of polydopamine, which exhibited several kinds of polydopamine structure with quinone groups [24]. As the RGPA reaction pH increased from 8 to 8.5, then to 10, the PWF values of the RGPA membrane increased from 644.77 L m^{-2} h^{-1} to 1823.97 L m^{-2} h^{-1} and then decreased to 53.72 L m^{-2} h^{-1} (Fig. 4d). There are two possible reasons for that phenomenon. First, the dopamine was rapidly oxidized to form PDA (indole-5,6-quinone) at a higher pH through the ring-closure reactions [35]. Second, it is because that the initial pH influenced the hydrolysis and condensation process of APTES. Here, the conductivity value of the RGPA mixture is a significant factor to reflect the hydrolysis extent of APTES. The conductivity values corresponding to the pH values of 8, 8.5, and 9.5 were 1242 μs/cm, 1396 μs/cm, and 1612 μs/cm, respectively. The APTES after hydrolysis can alter the conductivity property of RGPA aqueous solutions. The Si–O–CH_3 on APTES could be hydrolyzed to Si–OH partly in the RGPA aqueous solutions. In general, the conductivity is directly proportional to the contents of Si–OH. However, the Si–O–Si functional groups are usually formed *via* the condensation reaction of Si–OH functional groups on APTES. Therefore, the conductivity and stability of aqueous solutions decreased. Hence, with the increase of reaction pH, the condensation reaction was suppressed. Moreover, the result of the fit to the Si 2p spectra for RGPA composites synthesized at pH 7.5 and 9.5 environments was shown in Fig. S14 (Supporting information). Here, the data were fitted to two primary peaks, which were associated with O_3–Si–C and HO_3–Si–C at 102.4 eV and 102.9 eV, respectively [35]. The relative proportion of HO_3–Si–C increased from 18.42% to 38.06% as pH increases from 7.5 to 9.5. This observation is consistent with that of conductivity analysis that the more basic reaction condition is conducive to keep stable for the Si–OH groups and inhibits the condensation effect among them. The zeta potential and water angle measurements were also used to explore the pH effects on the preparation of RGPA composites. It can be seen in Fig. S15 (Supporting information) that with increase of preparation pH, the zeta potential for RGPA decreased. Meanwhile, as seen in Fig. S16 (Supporting information), the water contact angle of RGPA membrane decreased from 64.9° to 52.8° with the reaction pH value increasing from 7.5 to 9.5. All of these results might be ascribed to that at higher pH conditions, more Si–OH content increase the surface wettability (increase the hydrophilicity) and reduce the surface charge values. Hence, the cross-linking extent might be suppressed to some extent at higher pH reaction environment.

For the separation of MB and CR solutions (Figs. S13g and h in Supporting information), there is a discrepancy between MB and CR removal efficiencies. When the solution pH was at 8, the rejections of MB and CR solutions were 98.39% and 95.70%, respectively. Whereas the rejection of CR decreased to 90.18% as the pH increased to 8.5. It might be related to that the deprotonation role of phenolic on dopamine exhibited the negatively charged property at pH 8.5 [70]. Hence, the electrostatic repulsion effect between the anion CR solution and negatively RGPA composites restrained their interactions, which exhibited the decrease of CR rejection. With further increase of pH values, the fluxes of MB and CR had the same tendency with PWF values, that is, the fluxes demonstrated a great decrease. In contrast, the rejections of CR increased to 99.40% at a pH of 10. The observed increase in rejection for CR may be due to the decrease of flux, which favors the intercepting of the pollutants *via* the physical sieving effect. Here, based on the rejections and permeance of RGPA membranes, the pH of 8.5 was chosen for the optimized reaction.

Based on the optimization results of preparation conditions on the permeance and separation performances for RGPA membranes, the reaction conditions such as reaction cross-linker dosage, initial reaction pH, time, and temperature have significant effects on the structure formation and membrane arrangement manner. Among them, the cross-linker dosage acts as the crucial roles on the construction of membrane transport pathways. Hence, further experiments were based on the adjustment of cross-linker dosage to discuss the concrete membrane performances. Here, the reaction condition including 0.8 mL/L and 1.4 mL/L of APTES, the temperature of 80 °C, the time of 16 h, and the initial reaction pH of 8.5 for RGPA mixture, were selected for further experiments, respectively. The RGPA (0.8 mL/L) and RGPA (1.4 mL/L) composites filtrated on the CA membrane were defined as M1 and M2 membranes.

Moreover, membrane separation performance was related to the pollutant characteristic and the inner properties of membrane. To evaluate the membrane separation performance, the effect of dye pH, dye concentration, and the amount of filtration volumes on the separation performance of RGPA membrane were discussed. Moreover, the reusability, anti-fouling, and stability for RGPA membrane were also studied. The specific content was depicted as Text S5 (Supporting information).

All of these results revealed that RGPA membrane possessed a superior separation performance on the pollutants *via* tuning the interlayer nanochannel and nanostructure by crosslinker dosage. Based on the above investigations, we could conclude that the RGPA membrane with low cross-linking concentration was endowed the relatively high permeance and selectivity. The sieving effect was obvious at this condition. While, the high cross-linking concentration achieved high permeance and selectivity for MB, and relative weak selectivity for CR aqueous solutions. This drawback could be ameliorated by tuning the reaction pH, increasing the volume of casting solutions, and adjusting the pH of pollutants. All in all, in this work, we have put forward a controllable strategy to fabricate the inner structure of GO membrane to achieve the pu-

rification and effective separation of anionic and cationic dye pollutants.

As a type of superior membrane separation material, it is an essential procedure to clarify the separation mechanism of the RGPA membrane during the filtration process. In general, the separation mechanism includes physical sieving, electrostatic interaction, hydrogen bond, and π-π interaction effects [18,30,46,71]. First, the nanochannels assembled by the stacked GO membrane can intercept dye molecules during the filtration process, verified by the previous research [11,18,19]. Second, electrostatic interaction affects the separation performance because of the charge differences between membrane surface and dye aqueous solutions. Based on the results of zeta potential value (Fig. S17b in Supporting information), the RGPA composite is negatively charged in the pH range of 2–11. While our target pollutants such as MB and CR aqueous solutions are cationic and anionic materials, respectively. Thus, the electrostatic attraction interaction between RGPA material and MB molecules promotes the electrostatic adsorption of cationic dye molecules. This is consistent with previous investigations [11,46,71–73]. Meanwhile the removal of CR was due to the electrostatic repulsion between CR and RGPA composites. Third, the structures of MB and CR molecules are composed of benzene ring, amino, and sulfur functional groups (Fig. S27 in Supporting information). In terms of the structure characteristics for both dyes, the π-π and hydrogen bond effects might be also responsible for the separation of dye molecules during the filtration process. For the separation of MB molecules, the phenothiazines can also have interaction *via* the π-π interactions between MB and RGPA. CR is a disazo dye with a large conjugated system, which can form the π-π interactions *via* the benzene rings between the dyes and RGPA composites [74]. The FT-IR characterizations of RGPA composites before and after adsorption for MB and CR aqueous solutions at the pHs of 3, 5, 7, 9 and 11 verified the results. The C=C stretching peaks at 1618 cm^{-1} for both adsorbed materials shifting or demonstrating the abatement of peak intensity were also verified the π-π interactions between the dye molecules and RGPA composites (Figs. S28a and b in Supporting information) [75]. Finally, the hydrogen bond effect may occur between the hydroxyl, amino on RGPA composite and an azo double bond, N atoms, and S atoms on both dye molecules. Here, RGPA acted as the H-donor and the amino or sulfonic groups of dye molecules worked as the H-accepter [76–78]. The hydrogen effect between RGPA and dye molecules was also verified by previous research [75,79,80].

Hence, based on the previous investigations and our experiment results, it can be concluded that physical sieving, electrostatic interaction, π-π, and hydrogen bond were the separation mechanisms of MB and CR molecules for RGPA membrane. Differently, the physical sieving effect for RGPA membrane with higher crosslinker dosage was weaker than that of RGPA membrane with lower crosslinker dosage (lower water permeance). The membrane separation mechanism was depicted in Fig. S29 (Supporting information).

Fig. S30 (Supporting information) summarized the literature review of other modification GO membranes. Generally, the RGPA membrane possessed superior separation and permeance performances. The pure water flux of the RGPA membrane was 1823.97 L m^{-2} h^{-1}, which was far more than the pure water flux of other GO-based membranes [19,20,81–86]. Furthermore, the superior removal rates above 90% (CR) for RGPA membrane on dye aqueous solutions were also achieved. Hence, the RPGA membrane developed in this study showed great potentials for applications as membrane separation material in practical wastewater treatment.

In summary, covalent crosslink is a straightforward method to modify the interlayer gallery of GO membrane. In this study, a feasible fabrication approach to secondary covalent crosslink of GO membrane was carried out *via* the role of PDA and APTES to enhance its permeance and separation performances. The interlayer structure of RGPA was explored based on the optimization of the reaction conditions such as crosslinker concentration, reaction time, pH, and temperature. According to the optimization and characterization results, C–OH, C–O–C, and –COOH on the GO membrane served as the main active sites to interact with amide and hydroxyl on the network of PDA/APTES composite. The PDA/APTES grafting on GO membrane increases the surface roughness and promotes water permeance. A pure water flux of the RGPA membrane possessed high flux ranging from 11.98 L m^{-2} h^{-1} to 1823.97 L m^{-2} h^{-1}. The removal efficiencies of RGPA for MB and CR molecules were 99.17% and 90.18%, respectively. The separation mechanism for both dyes was ascribed to the physical sieving, electrostatic interaction, hydrogen bond, and π-π interaction effects. Moreover, the RGPA membrane demonstrated a great reusable performance, whose removal efficiency was still above 96.32% and 93.1% after 4 cycles for MB and CR aqueous solutions, respectively. Moreover, the M1 membrane exhibited superior antifouling properties with 75.98% of flux recovery ratio on BSA aqueous solution. Based on the above research, a cross-linking modification RGPA membrane with high permeance and excellent separation performances was developed. Therefore, the novel covalent cross-linking RGO/PDA/APTES membranes developed in this study offer great potentials for applications in wastewater treatment, salt/dye separation, water desalination, *etc.*

Declaration of competing interest

The authors declare no conflict of interest.

Acknowledgments

This study received financial support from the Sichuan Youth Science and Technology Innovation Research Team (No. 2020JDTD0018), the Regional Innovation Cooperation project of Sichuan Province (No. 2021YFQ0046), the Science and Technology Plan Project of Sichuan Province (No. 2019YJ0302), and the National Natural Science Foundation of China (No. 21707111). The Opening Project of Oil & Gas Field Chemistry Key Laboratory of Sichuan Province (No. YQKF202106). All tests were provided by the College of Chemistry and Chemical Engineering, Southwest Petroleum University.

Supplementary materials

Supplementary material associated with this article can be found, in the online version, at doi:10.1016/j.cclet.2022.03.045.

References

[1] W. Zheng, S. You, Y. Yao, et al., Appl. Catal. B: Environ. 298 (2021) 120593.
[2] W. Zheng, Y. Liu, W. Liu, et al., Water. Res. 194 (2021) 116961.
[3] D. Guo, Y. Liu, H. Ji, et al., Environ. Sci. Technol. 55 (2021) 4045–4053.
[4] L. Kumar, M. Chugh, S. Kumar, et al., Process Saf. Environ. Prot. 159 (2022) 362–375.
[5] X. Zhang, J. Membr. Sci. 643 (2022) 120052.
[6] G. Liu, W. Jin, N. Xu, Angew. Chem. Int. Ed. 55 (2016) 13384–13397.
[7] J. Hu, M. Li, L. Wang, et al., J. Membr. Sci. 618 (2021) 118698.
[8] Y. Gao, S. Yan, Y. He, et al., J. Membr. Sci. 626 (2021) 119192.
[9] A. Alkhouzaam, H. Qiblawey, J. Membr. Sci. 620 (2021) 118900.
[10] H. Zeng, Z. Yu, L. Shao, et al., Desalination 491 (2020) 114558.
[11] H. Deng, J. Huang, C. Qin, et al., J. Water. Process. Eng. 40 (2021) 101945.
[12] M. Zhang, K. Guan, Y. Ji, et al., Nat. Commun. 10 (2019) 1253.
[13] Y. Liu, W. Tu, M. Chen, et al., Chem. Eng. J. 336 (2018) 263–277.
[14] H. Yu, G. Xiao, Y. He, et al., Desalination 500 (2021) 114868.
[15] D.W. Kim, J. Choi, D. Kim, et al., J. Mater. Chem. A 4 (2016) 17773–17781.
[16] G. Liu, W. Jin, N. Xu, Chem. Soc. Rev. 44 (2015) 5016–5030.
[17] Y. Liu, D. Gan, M. Chen, et al., Sep. Purif. Technol. 253 (2020) 117552.
[18] H. Zeng, Z. Yu, L. Shao, et al., Chem. Eng. J. 403 (2021) 126281.
[19] N.A. Khan, J. Yuan, H. Wu, et al., ACS Appl. Mater. Interfaces 11 (2019) 28978–28986.

[20] S. Valizadeh, L. Naji, M. Karimi, Sep. Purif. Technol. 263 (2021) 118392.
[21] J.J. Lu, Y.H. Gu, Y. Chen, et al., Sep. Purif. Technol. 210 (2019) 737–745.
[22] X. Yang, L. Yuan, Y. Zhao, et al., J. Membr. Sci. 612 (2020) 118471.
[23] F. Li, Z. Yu, H. Shi, et al., Chem. Eng. J. 322 (2017) 33–45.
[24] Y. Liu, K. Ai, L. Lu, Chem. Rev. 114 (2014) 5057–5115.
[25] H. Shi, Y. He, Y. Pan, et al., J. Membr. Sci. 506 (2016) 60–70.
[26] Z. Jia, Y. Wang, W. Shi, et al., J. Membr. Sci. 520 (2016) 139–144.
[27] Z. Jia, Y. Wang, J. Mater. Chem. A 3 (2015) 4405–4412.
[28] J.M. Luque-Alled, A. Abdel-Karim, M. Alberto, et al., Sep. Purif. Technol. 230 (2020) 115836.
[29] Q. Gu, T.C.A. Ng, I. Zain, et al., Appl. Surf. Sci. 502 (2020) 144128.
[30] J. Ma, Y. He, X. Tang, et al., Sep. Purif. Technol. 266 (2021) 118067.
[31] Y. Zhan, J. Zhang, X. Wan, et al., Appl. Surf. Sci. 436 (2018) 756–767.
[32] G. Zeng, Z. Ye, Y. He, et al., Chem. Eng. J. 323 (2017) 572–583.
[33] J. Yuan, Z. Zhang, M. Yang, et al., Tribol. Int. 107 (2017) 10–17.
[34] L. Zhou, Y. He, H. Shi, et al., J. Hazard. Mater. 380 (2019) 120865.
[35] D.B. Knorr, N.T. Tran, K.J. Gaskell, et al., Langmuir 32 (2016) 4370–4381.
[36] J.Y. Lee, J.Y. Zhan, M.B.M.Y. Ang, et al., Sep. Purif. Technol. 265 (2021) 118470.
[37] S. Yang, Q. Zou, T. Wang, et al., J. Membr. Sci. 569 (2019) 48–59.
[38] F. Pan, Y. Li, Y. Song, et al., J. Membr. Sci. 595 (2020) 117486.
[39] Y. Xu, Q. Gao, H. Liang, et al., Polym. Test. 54 (2016) 168–175.
[40] Z. Wen, C. Xu, X. Qian, et al., Appl. Surf. Sci. 486 (2019) 546–554.
[41] W. Cui, M. Li, J. Liu, et al., ACS Nano 8 (2014) 9511–9517.
[42] X. Yan, L. Huo, C. Ma, et al., Process Saf. Environ. Prot. 130 (2019) 257–264.
[43] Y. Li, H. Zhang, P. Liu, et al., Small 9 (2013) 3336–3344.
[44] P. Bandyopadhyay, W.B. Park, R.K. Layek, et al., J. Membr. Sci. 500 (2016) 106–114.
[45] P. Bandyopadhyay, T. Kuila, J. Balamurugan, et al., Chem. Eng. J. 308 (2017) 1174–1184.
[46] X. Fan, C. Cai, J. Gao, et al., Sep. Purif. Technol. 241 (2020) 116730.
[47] X. Feng, B. Qiu, Y. Dang, et al., Chem. Eng. J. 412 (2021) 128710.
[48] R. Rajumon, J.C. Anand, A.M. Ealias, et al., J. Environ. Chem. Eng. 7 (2019) 103479.
[49] M. Thommes, K. Kaneko, A.V. Neimark, et al., Pure Appl. Chem. 87 (2015) 1051–1069.
[50] L. Yang, J. Kong, W.A. Yee, et al., Nanoscale 4 (2012) 4968–4971.
[51] L. Yang, W.A. Yee, S.L. Phua, et al., RSC Adv. 2 (2012) 2208–2210.
[52] Y. Zhang, K. Su, Z. Li, J. Membr. Sci. 563 (2018) 718–725.
[53] J. Feng, H. Fan, D.A. Zha, et al., Langmuir 32 (2016) 10377–10386.
[54] S. Li, Y. Wan, S. Guo, et al., Chem. Eng. J. 411 (2021) 128587.
[55] J. Yang, M.A. Cohen Stuart, M. Kamperman, Chem. Soc. Rev. 43 (2014) 8271–8298.
[56] F. Riedel, S. Spange, J. Phys. Org. Chem. 22 (2009) 203–211.
[57] Q. Wu, Q. Wan, X. Yang, et al., Compos. Sci. Technol. 205 (2021) 108648.
[58] Z. Yu, F. Li, Q. Yang, et al., ACS Sustain. Chem. Eng. 5 (2017) 7840–7850.
[59] F. Wang, S. Lin, X. Lu, et al., Electrochim. Acta 404 (2022) 139708.
[60] N. Sbirrazzuoli, A. Mititelu-Mija, L. Vincent, et al., Thermochim. Acta 447 (2006) 167–177.
[61] Z. Zhang, X. Xiao, Y. Zhou, et al., ACS Nano 15 (2021) 13178–13187.
[62] E. Igbinigun, Y. Fennell, R. Malaisamy, et al., J. Membr. Sci. 514 (2016) 518–526.
[63] J. Ma, X. Tang, Y. He, et al., Desalination 480 (2020) 114328.
[64] A. Abdel-Karim, S. Leaper, M. Alberto, et al., Chem. Eng. J. 334 (2018) 789–799.
[65] Y. Mansourpanah, A. Ghanbari, H. Yazdani, et al., Desalination 511 (2021) 115109.
[66] Y. Qian, X. Zhang, C. Liu, et al., Desalination 460 (2019) 56–63.
[67] C. Cheng, S. Li, S. Nie, et al., Biomacromolecules 13 (2012) 4236–4246.
[68] S. Yenisetti, L. Phom, M. Ayajuddin, Dopamine: Health and Disease, IntechOpen, Croatia, 2019.
[69] Y. Zhu, J. Wang, F. Zhang, et al., Adv. Funct. Mater. 28 (2018) 1804121.
[70] Z. Ma, X. Jia, J. Hu, et al., Langmuir 29 (2013) 5631–5637.
[71] M. Khansanami, A. Esfandiar, Environ. Res. 201 (2021) 111576.
[72] Z. Yang, Z. Yuan, Z. Shang, et al., Appl. Clay Sci. 197 (2020) 105781.
[73] W.J. Zeng, C. Li, Y. Feng, et al., J. Water. Process. Eng. 40 (2021) 101901.
[74] J. Su, S. He, Z. Zhao, et al., Colloids Surf. A 554 (2018) 227–236.
[75] B. Ren, J. Miao, S. Wang, et al., Adv. Powder Technol. 32 (2021) 1774–1784.
[76] W. Konicki, M. Aleksandrzak, E. Mijowska, Chem. Eng. Res. Des. 123 (2017) 35–49.
[77] S.W. Lv, J.M. Liu, H. Ma, et al., Microporous. Mesoporous. Mater. 282 (2019) 179–187.
[78] O.V. Ovchinnikov, S.V. Chernykh, M.S. Smirnov, et al., J. Appl. Spectrosc. 74 (2007) 809–816.
[79] I. Mantasha, H. Saleh, K. Qasem, et al., Inorg. Chim. Acta. 511 (2020) 119787.
[80] J. Tang, Y.F. Zhang, Y. Liu, et al., Sep. Purif. Technol. 252 (2020) 117445.
[81] N. Meng, W. Zhao, E. Shamsaei, et al., J. Membr. Sci. 548 (2018) 363–371.
[82] P. Zhang, J.L. Gong, G.M. Zeng, et al., Chem. Eng. J. 322 (2017) 657–666.
[83] S. Wei, Y. Xie, Y. Xing, et al., J. Membr. Sci. 582 (2019) 414–422.
[84] Y. Xu, M. Wu, S. Yu, et al., J. Membr. Sci. 586 (2019) 15–22.
[85] X. Zhang, H. Li, J. Wang, et al., J. Membr. Sci. 581 (2019) 321–330.
[86] J. Li, M. Hu, H. Pei, et al., J. Membr. Sci. 595 (2020) 117547.